Layer-by-Layer Assembled Oxide Nanoparticle Electrodes with High Transparency, Electrical Conductivity, and Electrochemical Activity by Reducing Organic Linker-Induced Oxygen Vacancies

Ikjun Cho, Yongkwon Song, Sanghyuk Cheong, Younghoon Kim,* and Jinhan Cho*

Solution-processable transparent conducting oxide (TCO) nanoparticle (NP)–based electrodes are limited by their low electrical conductivity, which originates from the low level of oxygen vacancies within NPs and the contact resistance between neighboring NPs. Additionally, these electrodes suffer from the troublesome trade-off between electrical conductivity and optical transmittance and the restricted shape of substrates (i.e., only flat substrates). An oxygen-vacancy-controlled indium tin oxide (ITO) NP-based electrode is introduced using carbon-free molecular linkers with strong chemically reducing properties. Specifically, ITO NPs are layer-by-layer assembled with extremely small hydrazine monohydrate linkers composed of two amine groups, followed by thermal annealing. This approach markedly improves the electrical conductivity of ITO NP-based electrodes by significantly increasing the level of oxygen vacancies and decreasing the interparticle distance (i.e., contact resistance) without sacrificing optical transmittance. The prepared electrodes surpass the optical/electrical performance of TCO NP-based electrodes reported to date. Additionally, the nanostructured ITO NP films can be applied to more complex geometric substrates beyond flat substrates, and furthermore exhibit a prominent electrochemical activity. This approach can provide an important basis for developing a wide range of highly functional transparent conducting electrodes.

1. Introduction

Solution-processable transparent conducting oxide (TCO) electrodes, which can have high optical transparency, good electrical conductivity, and excellent operational stability in air, are

strongly required for the development of various optoelectronic and/or electrochemical applications with the desired geometries and flexibilities.[1–4] In line with such demands, many efforts have been focused on the preparation of TCO nanoparticles (NPs) and the development of their optimal solution approaches.[5–15] Generally, high-quality and monodisperse TCO NPs, including indium tin oxide (ITO), indium zinc oxide, aluminum-doped zinc oxide, and gallium-doped zinc oxide, have been synthesized using bulky/insulating organic ligands (e.g., oleic acid, oleylamine, tetrabutylammonium hydroxide) in organic media,[5–9] and the resultant TCO NP–based electrodes have been successfully prepared through inkjet printing, roll-to-roll deposition, and spin coating of TCO NPs onto flat glass substrates.[5–14] However, despite such progress, a few important factors need to be further considered for the preparation of next-generation TCO NP–based electrodes.

First, TCO NP films exhibit a low electrical conductivity because of the large amount of insulating organic ligands (i.e., bulky native ligands bound and/or unbound to the surface of TCO NPs) existing within the films and the low level of n-type dopant-like oxygen vacancies existing within the synthesized TCO NPs.[8,9,14] Considering that the presence of bulky organic ligands and the level of oxygen vacancies within TCO NPs are closely related to the contact resistance (or separation distance) between neighboring NPs and the intrinsic electrical conductivity of NPs, respectively, a high annealing temperature (>400 °C) under H_2 gas-containing inert condition is required for both the thermal decomposition of residual organics and the increase of oxygen vacancies.[5–9] However, partially decomposed organic residues still exist between neighboring TCO NPs even after thermal annealing, which consequently imposes limitations on further enhancements in the electrical performance of those electrodes. Although it has been reported that defect engineering strategies such as laser-assisted photothermal effect and reducing agent ($NaBH_4$)–assisted thermal treatment can be used for increasing the oxygen vacancies of metal oxides,[16,17] photothermal approach has much difficulty in significantly

Dr. I. Cho, Y. Song, Dr. S. Cheong, Prof. J. Cho
Department of Chemical and Biological Engineering
Korea University
145 Anam-ro, Seongbuk-gu, Seoul 02841, Republic of Korea
E-mail: jinhan71@korea.ac.kr
Dr. Y. Kim
Division of Energy Technology
Materials Research Institute
Daegu Gyeongbuk Institute of Science and Technology (DGIST)
333 Techno Jungang-daero, Hyeonpung-myeon, Dalseong-gun
Daegu 42988, Republic of Korea
E-mail: younghoon.kim@dgist.ac.kr

**ADVANCED
SCIENCE NEWS**

www.advancedsciencenews.com

NANO · MICRO

small

www.small-journal.com

increasing electrical conductivity due to the presence of residual organics, and furthermore the use of $NaBH_4$ can destabilize the NP electrodes by absence of organic linkers. Second, solution-processed TCO NP films requiring high annealing temperature have a complex and troublesome trade-off between electrical conductivity and optical transmittance. In most cases, hydrocarbon-based organics (including bulky native ligands) cause a light absorption due to the formation of carbon ashes after thermal decomposition, which significantly decreases the optical transmittance of the resultant TCO NP films.[18] Finally, the previously reported solution approaches, mainly based on spin coating or inkjet printing, can be applied to only flat substrates instead of complex geometric substrates including high-curvature substrates.[5–12] Therefore, the development of a more effective and unique approach is strongly required for the preparation of high-performance TCO NP–based electrodes with the desired geometries.

Here, we report an oxygen vacancy–controlled TCO NP–based electrode using the extremely small and carbon-free molecular linkers with a chemically reducing property. We also demonstrate that our approach can significantly alleviate the trade-off between electrical conductivity and optical transmittance of TCO NP films, producing a large number of oxygen vacancies within TCO NPs, and furthermore can be easily applied to highly curved substrates. For this study, ITO NPs were layer-by-layer (LbL)-assembled with carbon-free hydrazine monohydrate molecules ($H_2N-NH_2 \cdot H_2O$; hereafter, "Hyd") with an extremely small molecular weight ($M_w \approx 50$) and a chemically reducing property (**Figure 1**a). LbL assembly has been demonstrated as a well-established methodology for preparing nanocomposite films with tailored thicknesses, chemical compositions, and functionalities.[19–29] Although Hyd has been widely used as a chemically reducing agent (for example, in the preparation of reduced graphene oxide by chemical reduction
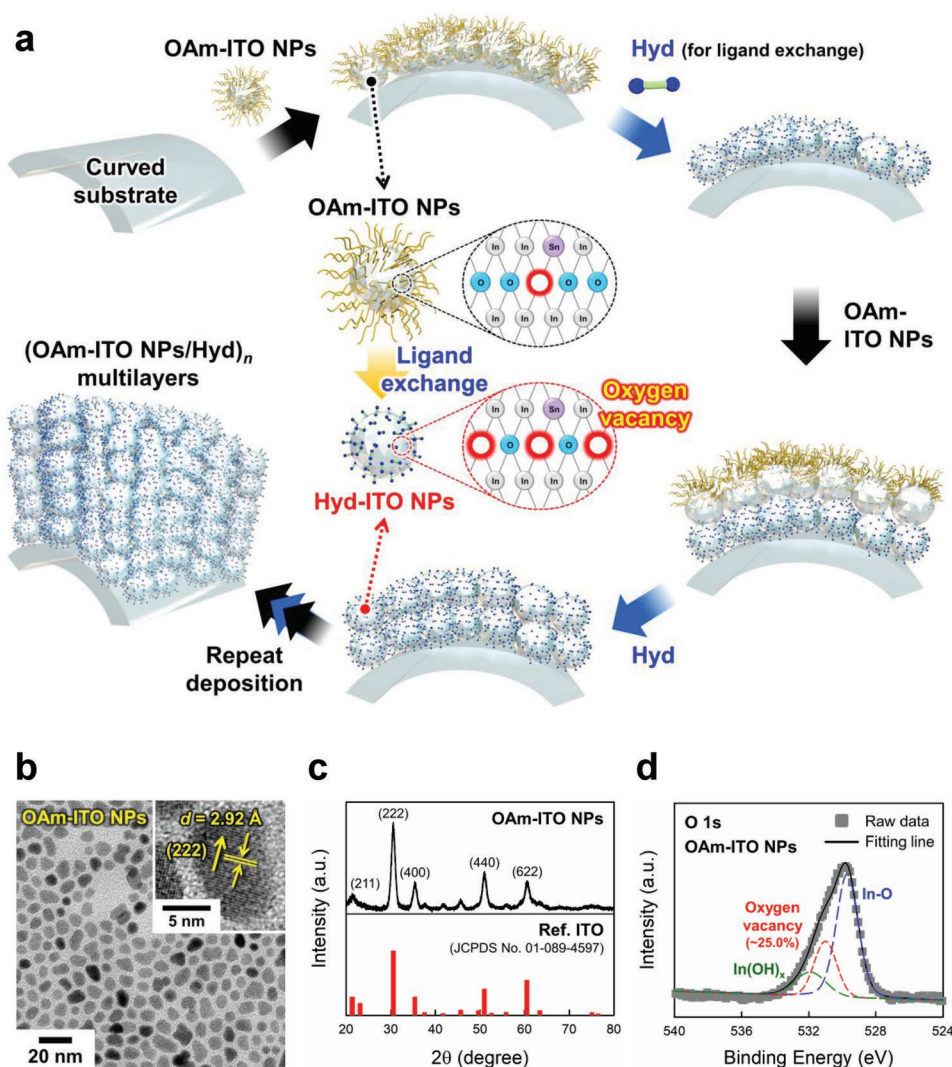
Figure 1. a) Schematic illustration of the preparation of ITO NP–based TCO electrodes by NH_2-functionalized molecular hydrazine linker–mediated LbL assembly. b) HR-TEM images of prepared OAm–ITO NPs dispersed in toluene. The inset shows the lattice spacing (*d*) measured to be ≈2.92 Å, which agreed with the (222) plane of ITO. c) XRD patterns of OAm–ITO NPs (top) and ITO reflections (bottom: JCPDS No. 01-089-4597). d) Deconvoluted XPS spectra of O 1s collected from OAm–ITO NPs.

of graphene oxide), it should be noted here that the Hyd used in this study are employed as a molecular linker for LbL assembly, which is evidently distinguished from previous LbL assemblies using bulky and insulating polymer linkers.

The smallest Hyd linkers composed of two primary amine (NH_2) groups can directly bridge vertically adjacent ITO NPs by substituting the bulky native ligands (i.e., oleylamine (OAm)) on the surface of ITO NPs, which can significantly decrease the contact resistance between neighboring ITO NPs. Particularly, these chemically reducing Hyd linkers notably increase the oxygen vacancy states of ITO NPs without any additional treatment during LbL depositions, and furthermore can effectively suppress the degradation of optical transmittance even after thermal annealing process due to their carbon-free property. The formed ITO NP films exhibited a significantly low sheet resistance ($\approx$86 Ω sq^{-1}) and a high optical transmittance ($\approx$90%) at an annealing temperature of 300 °C, which outperformed the electrical/optical properties of previous reports at the same or higher annealing temperature.[5–9,12] Unlike traditional fabrication methods, our approach could be effectively applied to highly curved substrates such as spherical glasses. Finally, for demonstrating the effectiveness and applicability of our approach, we showed that the nanostructured ITO NP–based TCO films can be used as a high-performance transparent energy-storage electrode due to their large active area and high electrical conductivity. Considering that the interparticle distance and oxygen vacancies are important factors for determining the performance of metal oxide NP–based films, we believe that our approach can be widely applied to other metal oxide NP–based applications as well as ITO NP–based TCO electrodes.

2. Results and Discussion

2.1. Preparation of (OAm-ITO NPs/Hyd)$_n$ Multilayers

For the preparation of TCO NP–based electrodes, we synthesized highly uniform OAm and octanoic acid (OCA)-stabilized indium tin oxide NPs with a tin (Sn) doping concentration of 9.2% and a diameter of 7.0 ± 2.4 nm (Figure 1b and Figure S1 and Table S1 (Supporting Information)).[30] The synthesized ITO NPs are briefly designated as OAm–ITO NPs because the mole amount of the used OAm ligands was much higher than that of OCA ligands. These OAm–ITO NPs were well-dispersed in nonpolar solvents, such as hexane and toluene (Figure S2, Supporting Information). As confirmed by high-resolution transmission electron microscopy (HR-TEM), the prepared OAm–ITO NPs displayed well-defined crystal structures with a lattice spacing (d) of 2.92 Å (the inset of Figure 1b). Additionally, the obvious (222), (400), and (440) peaks in the X-ray diffraction (XRD) patterns indicated that the OAm–ITO NPs have a basic In_2O_3 cubic bixbyite structure and high crystallinity (based on the JCPDS card No. 01-089-4597 ($In_{1.875}O_3Sn_{0.125}$), Figure 1c).[31,32]

To better understand the chemical states of the synthesized OAm–ITO NPs, we further investigated the binding energies of OAm–ITO NPs using X-ray photoelectron spectroscopy (XPS) (Figure 1d and Figure S3 (Supporting Information)). As

shown in Figure 1d, the oxygen (O) atom 1s spectrum could be divided by three deconvoluted peaks that originate from the lattice oxygen of the crystalline ITO NPs (529.7 eV; O atomic states: $\approx$60.0%), oxygen vacancy states (531.0 eV; $\approx$25.0%), and surface hydroxyl groups (531.9 eV; $\approx$15.0%). Given that oxygen vacancy states can act as n-type dopants, the relatively low ratio of oxygen vacancy states in the synthesized OAm–ITO NPs leads to considerable difficulty in generating the high electrical conductivity required for TCO electrodes. Furthermore, bulky native OAm and OCA ligands bound to the surface of ITO NPs increased the separation distance (i.e., contact resistance) between neighboring ITO NPs, and consequently, the solution-cast OAm–ITO NP films exhibited insulating properties (sheet resistance $\gtrsim$ 10^8 Ω sq^{-1}). Therefore, we needed to develop a novel approach to increase the oxygen vacancy states in the OAm–ITO NPs and to minimize the separation distance between neighboring ITO NPs for the preparation of functional ITO NP–based TCO electrodes.

To resolve these critical problems, OAm–ITO NPs were LbL-assembled with Hyd molecules that can operate as the strong chemically reducing agents as well as the small organic linkers. Interestingly, the bulky native ligands (i.e., OAm and OCA ligands), which are loosely bound to the surface of ITO NPs, are replaced by Hyd molecules through successive ligand-exchange reactions by the high affinity between the bare surface of ITO NPs and the NH_2 groups of Hyd during LbL assembly. More specifically, the presence of residual native ligands in the LbL-assembled (OAm–ITO NPs/Hyd)$_n$ multilayers (where n represents the number of bilayers) was examined by Fourier transform infrared (FTIR) spectroscopy in attenuated total reflection (ATR) mode (**Figure 2**a). The FTIR spectrum of pristine OAm–ITO NPs exhibited distinct absorption peaks originating from C—H stretching (by the long alkyl chains of OAm and OCA ligands) at 2927 and 2850 cm^{-1}, respectively, whereas the spectrum of pristine Hyd had no apparent absorption peaks in the same wavelength region (Figure S4, Supporting Information).[33] Therefore, when the OAm–ITO NPs were deposited onto NH_2-functionalized substrates (i.e., poly(ethylene imine) (PEI)-coated substrates), two noticeable C—H stretching peaks were observed in the spectrum of the OAm–ITO NP layer–coated substrates (see the FTIR spectrum referred to as "0.5 bilayers" in Figure 2a). Subsequently, as Hyd molecules were adsorbed onto the OAm–ITO NP layer–coated substrates, the C—H stretching peaks became barely detectable (see the FTIR spectrum referred to as "1 bilayers" in Figure 2a), indicating successful ligand-exchange reactions between the bulky OAm/OCA ligands and Hyd linkers. Therefore, the alternating deposition of OAm–ITO NPs and Hyd molecules continually induced the disappearance and regeneration of the C—H stretching peaks, forming the (OAm–ITO NPs/Hyd)$_n$ multilayers.

Based on these results, we qualitatively investigated the vertical growth of (OAm–ITO NPs/Hyd)$_n$ multilayers as a function of bilayer number (n) using UV–visible spectroscopy (Figure 2b). The absorbance of (OAm–ITO NPs/Hyd)$_n$ multilayers linearly increased with increasing bilayer number, and the formed ITO NP films had no absorption in a visible wavelength region ranging from 400 (3.1 eV) to 800 nm (1.55 eV) owing to their wide optical bandgap ($E_g \approx$ 4.08 eV) (Figure S5,
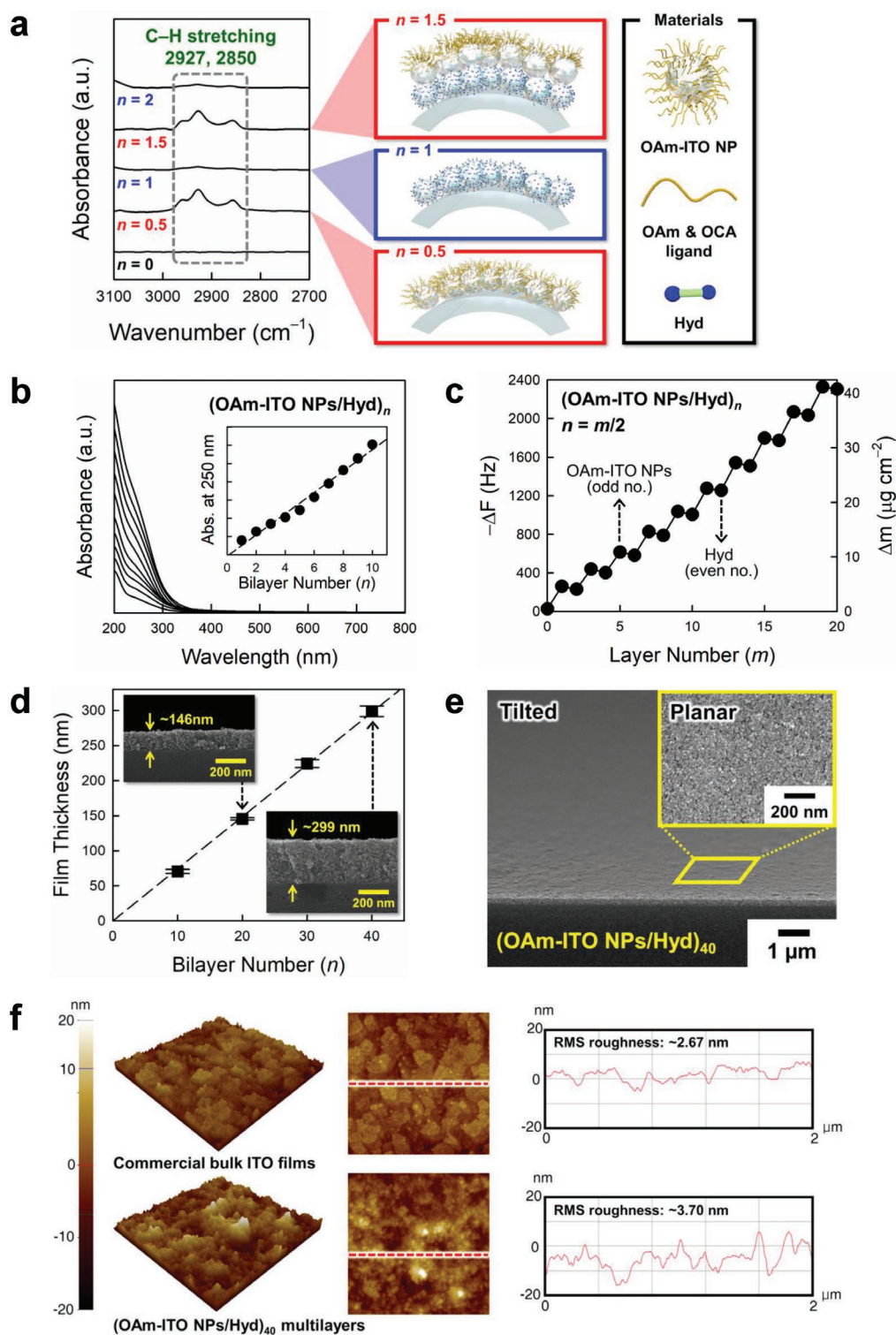
Figure 2. a) ATR–FTIR spectra and schematic representations of LbL-assembled (OAm–ITO NPs/Hyd)$_n$ multilayers on gold-sputtered Si wafers as a function of bilayer number (n). b) UV–visible absorbance spectra of (OAm–ITO NPs/Hyd)$_n$ multilayers on glasses with increasing bilayer number. The inset shows the absorbance at a wavelength of 250 nm, which exhibits a regular and uniform growth of the multilayers. c) Frequency and mass changes according to the alternating deposition of (OAm–ITO NPs/Hyd)$_n$ multilayers obtained from QCM measurements. Odd and even layer numbers correspond to the deposition of OAm–ITO NPs and Hyd, respectively. d) Total thickness change of (OAm–ITO NPs /Hyd)$_n$ multilayers on Si wafers measured from cross-sectional FE-SEM images (insets) as a function of bilayer number. e) Tilted and planar (inset) FE-SEM images of (OAm–ITO NPs/Hyd)$_{40}$ multilayers on Si wafers. f) AFM images (left; scan range: 2 µm × 2 µm) and height profiles (right; height profile analysis obtained from the red dashed line of the AFM images) of commercial bulk ITO films (top panel) and (OAm–ITO NPs/Hyd)$_{40}$ multilayers (bottom panel).

Supporting Information), which almost coincided with that of commercial bulk ITO films (E_g: 3.5–4.3 eV).[34] We also quantitatively examined the loading amount of (OAm–ITO NPs/Hyd)$_n$ multilayers using quartz crystal microgravimetry (QCM) (Figure 2c). Assuming that the layers were rigid and sufficiently thin to satisfy the Sauerbrey equation, the mass changes (Δm) were calculated from the frequency changes ($-\Delta F$) caused by the adsorption of (OAm–ITO NPs/Hyd) bilayers onto the QCM electrode (a more detailed explanation is given in the Experimental Section). The loading amount of (OAm–ITO NPs/Hyd) bilayers resulted in a $-\Delta F$ of 240.8 ± 12.0 Hz, which corresponded to a Δm of 4.0 ± 0.5 µg cm^{-2} per bilayer. The slight decrease in the mass changes during the deposition of Hyd implied that the bulky native OAm ($M_w \approx 267$) and OCA ($M_w \approx 144$) ligands were replaced by the smaller Hyd molecules ($M_w \approx 50$). In line with the increase of ITO NP loading mass, the total thickness of (OAm-ITO NPs/Hyd)$_n$ multilayers linearly increased from ≈70 to 299 nm with increasing bilayer number 10 to 40, forming a highly uniform and smooth morphology as observed by field-emission scanning electron microscopy (FE-SEM) (Figure 2d,e). The root-mean-square surface roughness of (OAm–ITO NPs/Hyd)$_{40}$ multilayers obtained from atomic force microscopy (AFM) was measured to be ≈3.70 nm, which is comparable to that of commercial bulk ITO films prepared from sputtering process (≈2.67 nm) (Figure 2f). Additionally, it should be here noted that the Hyd linkers can also be LbL-assembled with hydrophobic metal NPs, such as tetraoctylammonium (TOA)-stabilized Au or Ag NPs (in brief, TOA–Au and Ag NPs), indicating a versatile applicability of Hyd linkers for the preparation of metal and/or metal oxide nanocomposite films (Figure S6, Supporting Information).

2.2. (OAm–ITO NPs/Hyd)$_n$ Multilayer–Based TCO Electrodes

On the basis of the successful preparation of (OAm–ITO NPs/Hyd)$_n$ multilayers in the previous section, we then sought to use these films to construct TCO electrodes. The (OAm–ITO NPs/Hyd)$_{40}$ film, with the minimized separation distance between neighboring ITO NPs by the use of Hyd linkers, exhibited the sheet resistance of 4.7×10^5 Ω sq^{-1}. Although the solution-cast OAm–ITO NP films or (OAm–ITO NPs/bulky polymer linker)$_n$ multilayers had almost insulating properties ($\gtrsim 10^8$ Ω sq^{-1}) (the more detailed explanation will be given in the latter part), the (OAm–ITO NPs/Hyd)$_{40}$ multilayers displayed a notably enhanced electrical property. However, it was still unsuitable for use as a TCO electrode. To further improve the electrical conductivity, the (OAm–ITO NPs/Hyd)$_n$ multilayers deposited onto glass substrates were thermally annealed at 300 °C in an inert atmosphere (95% Ar and 5% H$_2$ gas). This thermal annealing process was conducted to increase the ratio of oxygen vacancy states in the ITO NPs.

Figure 3a shows the sheet resistance and the optical transmittance of (OAm–ITO NPs/Hyd)$_n$ multilayer–coated glasses thermally annealed at 300 °C as a function of bilayer number (n). Upon increasing the bilayer number from 10 to 40, the sheet resistance markedly decreased from 4.1×10^5 to 86 Ω sq^{-1} (electrical conductivity: ≈389 S cm^{-1}; resistivity: ≈2.6×10^{-3} Ω cm). Additionally, the optical transmittance of the

(OAm–ITO NPs/Hyd)$_n$ multilayers was maintained in the range of 90.0–89.6% at a visible wavelength of 550 nm. Although Lee et al. also prepared the solution-processed ITO NP films using spin coating, their reported sheet resistance was ≈400% higher than that of our LbL-assembled ITO NP films despite the same annealing temperature.[5] The change in the sheet resistance of (OAm–ITO NPs/Hyd)$_{40}$ multilayers as a function of annealing temperature is also shown in Figure 3b. When the annealing temperature increased from 25 to 300 °C, the sheet resistance of the multilayers decreased from 4.7×10^5 to 86 Ω sq^{-1} (Figure S7, Supporting Information). In particular, upon increasing the annealing temperature from 300 to 400 °C, it should be noted that the sheet resistance of the multilayers could be further decreased up to 30 Ω sq^{-1} (electrical conductivity: ≈1.1×10^3 S cm^{-1}; resistivity: ≈9.0×10^{-4} Ω cm), outperforming the optical/electrical properties of ITO NP–based TCO electrodes reported to date (Figure S8 and Table S2, Supporting Information).

The remarkable electrical performance of our ITO NP–based TCO electrodes is attributed to the use of the smallest and chemically reducing Hyd linkers that bridged between adjacent ITO NPs. To confirm this possibility, we examined the electrical properties of (OAm–ITO NPs/linker)$_{40}$ multilayers prepared from three different NH$_2$-functionalized organic linkers (i.e., PEI ($M_w \approx 800$), tris(2-aminoethyl)amine (TREN, $M_w \approx 146$), and Hyd ($M_w \approx 50$)). As an organic linker, NH$_2$-functionalized PEI (or TREN) is also LbL-assembled with OAm–ITO NPs through ligand-exchange reactions between the native ligands on the ITO NPs and the NH$_2$ groups of PEI (or TREN). The PEI and TREN linker–based multilayers exhibited the higher loading amount of ITO NPs per bilayer (≈5.82 and ≈5.02 µg cm^{-2}, respectively) than the Hyd linker–based multilayers (≈3.83 µg cm^{-2}), which resulted from their relatively many binding sites (i.e., NH$_2$ groups) for the adsorption of ITO NPs compared to those of Hyd (Figures S9 and S10, Supporting Information). Additionally, the formed (OAm–ITO NPs/PEI)$_{40}$ and (OAm–ITO NPs/TREN)$_{40}$ multilayers displayed a thicker film thickness (≈447 and ≈410 nm, respectively) than the (OAm–ITO NPs/Hyd)$_{40}$ multilayers (≈299 nm) (Figure S11, Supporting Information). However, despite the low loading amount (or film thickness) of conductive ITO NP films, the (OAm–ITO NPs/Hyd)$_{40}$ multilayers exhibit a higher electrical conductivity of ≈389 S cm^{-1} and a lower sheet resistance of ≈86 Ω sq^{-1} at an annealing temperature of 300 °C (Figure 3c). By contrast, the (OAm–ITO NPs/PEI)$_{40}$ and (OAm–ITO NPs/TREN)$_{40}$ multilayers exhibited the lower electrical conductivities of 0.097 S cm^{-1} (sheet resistance: ≈2.3×10^5 Ω sq^{-1}) and 70.5 S cm^{-1} (sheet resistance: ≈346 Ω sq^{-1}), respectively (Table S3, Supporting Information). It should be noted here that the solution-cast OAm–ITO NP films without LbL assembly had an insulating property even after thermal annealing at 300 °C due to the presence of bulky native ligands bound to the surface of ITO NPs. This superior electrical performance of (OAm–ITO NPs/Hyd)$_n$ multilayers implies that the size of organic linkers directly affects the electron transfer (or contact resistance) between neighboring ITO NPs. To our knowledge, Hyd molecules are the smallest NH$_2$-functionalized organic linkers that can act as a bridge between vertically adjacent TCO NPs including ITO NPs.
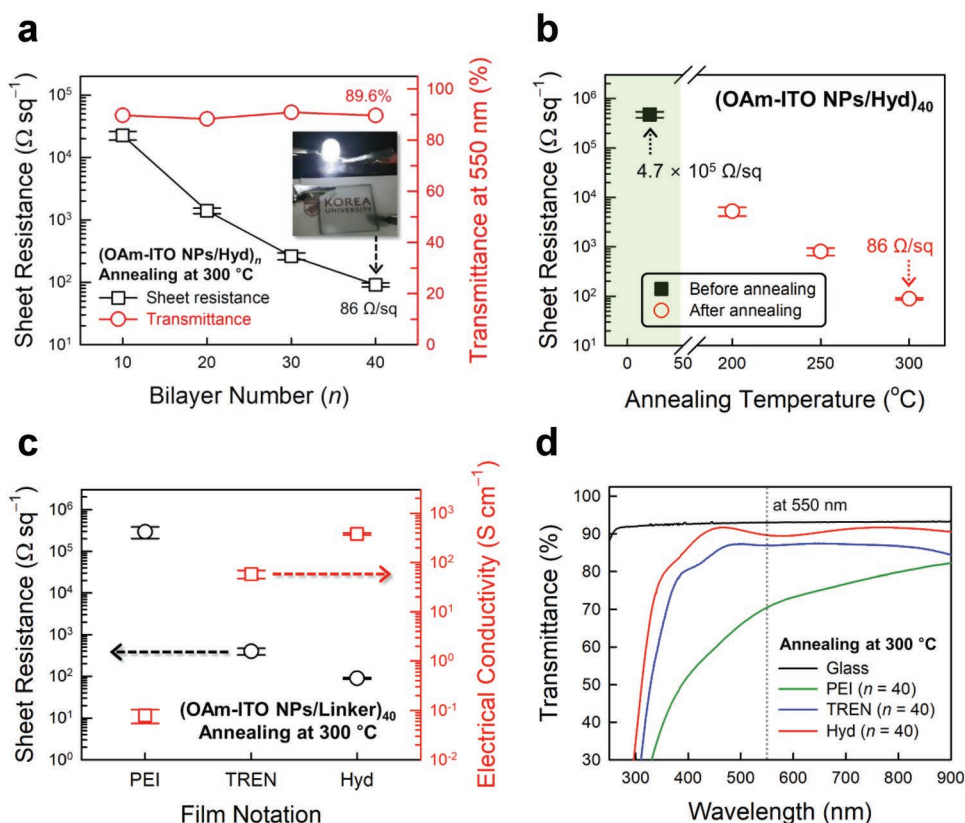
Figure 3. a) Sheet resistance (left axis, black squares) and optical transmittance at 550 nm (right axis, red circles) of (OAm–ITO NPs/Hyd)$_n$ multilayers on glasses after thermal annealing at 300 °C as a function of bilayer number (n). The inset shows a photograph of (OAm–ITO NPs/Hyd)$_{40}$ multilayers on a glass connected with an LED. b) Sheet resistance of (OAm–ITO NPs/Hyd)$_{40}$ multilayers on glasses before and after thermal annealing as a function of annealing temperature, which is varied from 200 to 300 °C. c) Sheet resistance (left axis, black circles) and electrical conductivity (right axis, red squares) of (OAm–ITO NPs/linker)$_{40}$ multilayer–coated glasses after thermal annealing at 300 °C. In this case, PEI, TREN, and Hyd were used as organic linkers that bridged between vertically adjacent ITO NPs. d) Optical transmittance spectra of (OAm–ITO NPs/linker)$_{40}$ multilayers (linker: PEI, TREN, and Hyd) on glasses after thermal annealing at 300 °C.

Another important benefit of Hyd linkers is that (OAm–ITO NPs/Hyd)$_{40}$ multilayers maintained a high optical transmittance of ≈90% at a wavelength of 550 nm even after thermal annealing at 300 °C (Figure 3d). In this case, a little hump with maxima and minima in the transmittance spectra of (OAm–ITO NPs/Hyd)$_{40}$ multilayers was caused by the interferences at different wavelengths.[35,36] On the other hand, the optical transmittance of thermally annealed (OAm–ITO NPs/PEI)$_{40}$ and (OAm–ITO NPs/TREN)$_{40}$ multilayers decreased by 19.5% and 2.9%, respectively, relative to their initial transmittance values before thermal annealing (Table S3, Supporting Information). These degradations of optical transmittance in the PEI and TREN linker–based multilayers mainly occurred from the thermal decomposition of hydrocarbon-based organic linkers.[18] As a result, the carbon-free Hyd linkers could minimize the degradation in the optical transmittance of (OAm–ITO NPs/Hyd)$_{40}$ multilayers after thermal annealing.

Furthermore, given that Hyd is a well-known strong reducing agent,[37] it was assumed that Hyd would contribute to the increase in the oxygen vacancy states of ITO NPs related to the electrical conductivity. To verify this possibility, we investigated the oxygen vacancy states in the ITO NPs that were LbL-assembled with NH$_2$-functionalized PEI, TREN, and Hyd

linkers (**Figure 4**a,b and Figure S12 (Supporting Information)). The ratios of oxygen vacancies in the (OAm–ITO NPs/Hyd)$_{40}$ multilayers before and after thermal annealing at 300 °C were estimated to be ≈36% and 59%, respectively, which exceeded those of solution-cast OAm–ITO NP films (oxygen vacancy ≈25% and ≈33%, respectively), PEI linker (oxygen vacancy ≈27% and ≈33%, respectively), and TREN linker (oxygen vacancy ≈32% and ≈42%, respectively)-based multilayers at the same annealing conditions. These results imply that the ratio of oxygen vacancies in metal oxide NPs, such as ITO NPs, can be significantly increased with an aid of small organic linkers operating as strong reducing agents. Additionally, the presented LbL assembly method enables the preparation of TCO NP–based electrodes on highly curved substrates using dipping process (Figure 4c and Video S1 (Supporting Information)). More specifically, when the (OAm–ITO NPs/Hyd)$_{40}$ multilayers were deposited onto a transparent spherical glass substrate and then thermally annealed at 300 °C, the light-emitting diode (LED) connected to the ITO NP multilayer–coated spherical glass was illuminated in all positions on the spherical TCO electrode. That is, our approach transformed an insulating spherical glass into the transparent conducting spherical electrode. Given that solution-based approaches for TCO electrodes reported to
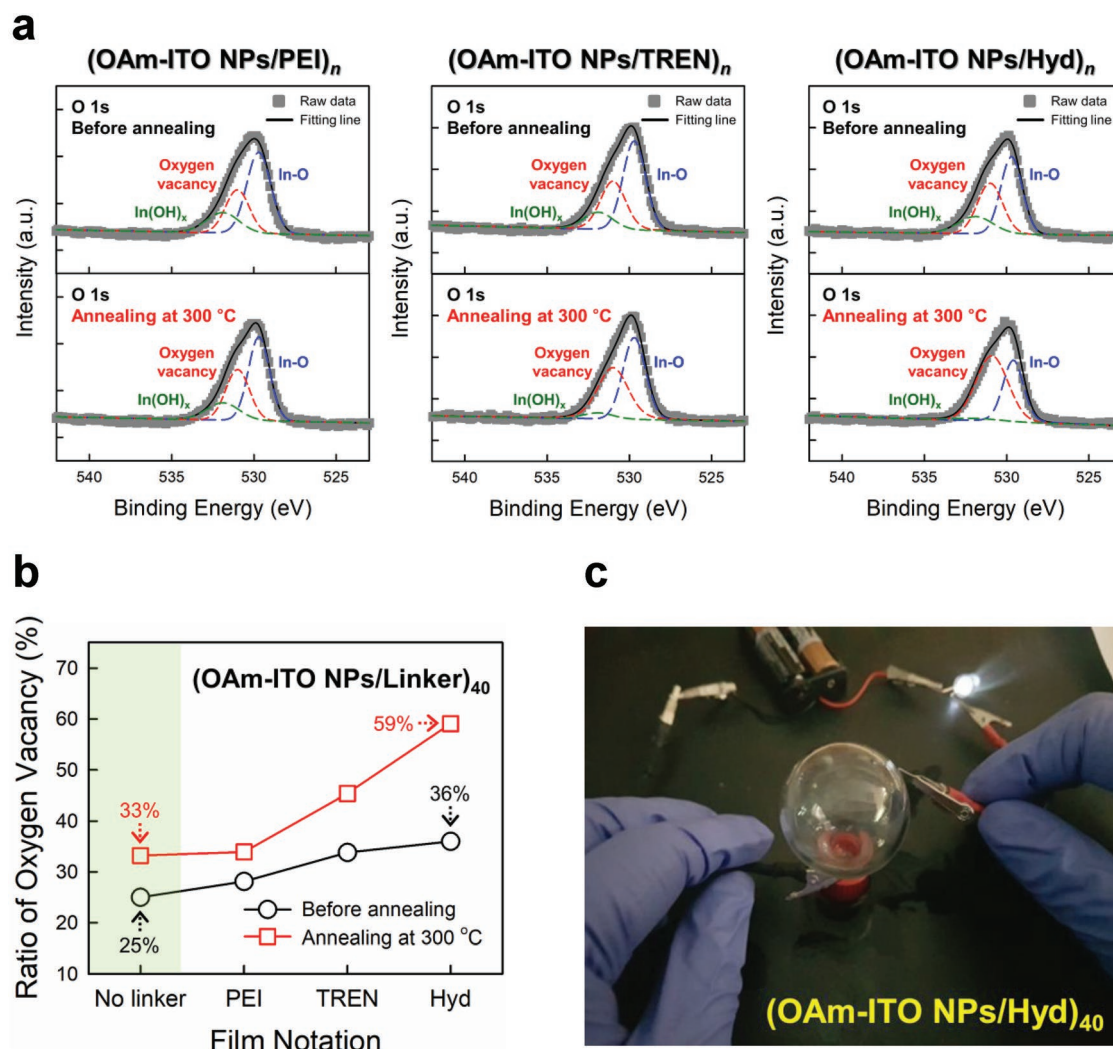
Figure 4. a) Deconvoluted XPS spectra of O 1s peaks collected from (OAm–ITO NPs/linker)$_{40}$ multilayers (linker: PEI, TREN, and Hyd) before (top) and after (bottom) thermal annealing at 300 °C. b) Ratio of oxygen vacancies for (OAm–ITO NPs/linker)$_{40}$ multilayers with three different linkers before and after thermal annealing at 300 °C. c) Photographic image of (OAm–ITO NPs/Hyd)$_{40}$ multilayers on a high-curvature bulb glass connected with an LED after thermal annealing at 300 °C.

date have focused on flat substrates, our approach that is not restricted by the size, shape, and type of substrates can provide an important basis for preparing next-generation TCO electrodes with the desired geometries.

2.3. Electrochemical Properties of (OAm–ITO NPs/Hyd)$_n$ Multilayers

To further demonstrate the effectiveness and applicability of our approach, we investigated the electrochemical performance of (OAm–ITO NPs/Hyd)$_n$ multilayers as transparent energy-storage electrodes. For this study, the (OAm–ITO NPs/Hyd)$_n$ multilayers were deposited onto commercial ITO–sputtered glass substrates (current collectors) and then thermally annealed at 300 °C under an inert atmosphere with 5% H_2 gas. After these processes, the charge storage characteristics of the (OAm–ITO NPs/Hyd)$_n$ multilayers were examined in

a three-electrode cell configuration containing a 0.5 M Na_2SO_4 electrolyte at room temperature. First, cyclic voltammetry (CV) scans of (OAm–ITO NPs/Hyd)$_n$ multilayers were conducted at a scan rate of 0.5 V s^{-1} in the potential range between −0.2 and +0.8 V with increasing bilayer number from 10 to 40 (**Figure 5**a). The current levels of the CV curves gradually increased in proportion to the bilayer number, which implied that the charge storage capabilities of the (OAm–ITO NPs/Hyd)$_n$ multilayers can be controlled and further scaled by simply adjusting the bilayer number. Additionally, almost quasirectangular-shaped CV curves without evident redox peaks were observed, indicating that the (OAm–ITO NPs/Hyd)$_n$ multilayers exhibited electric double-layer capacitor (EDLC) behaviors with fast current responses. In contrast, the bare ITO–sputtered glass substrates (thickness of bulk ITO films: ≈200 nm) displayed a negligible capacitance compared to the (OAm–ITO NPs/Hyd)$_n$ multilayers, which suggested that the charge storage capabilities shown in Figure 5a were entirely attributable to the
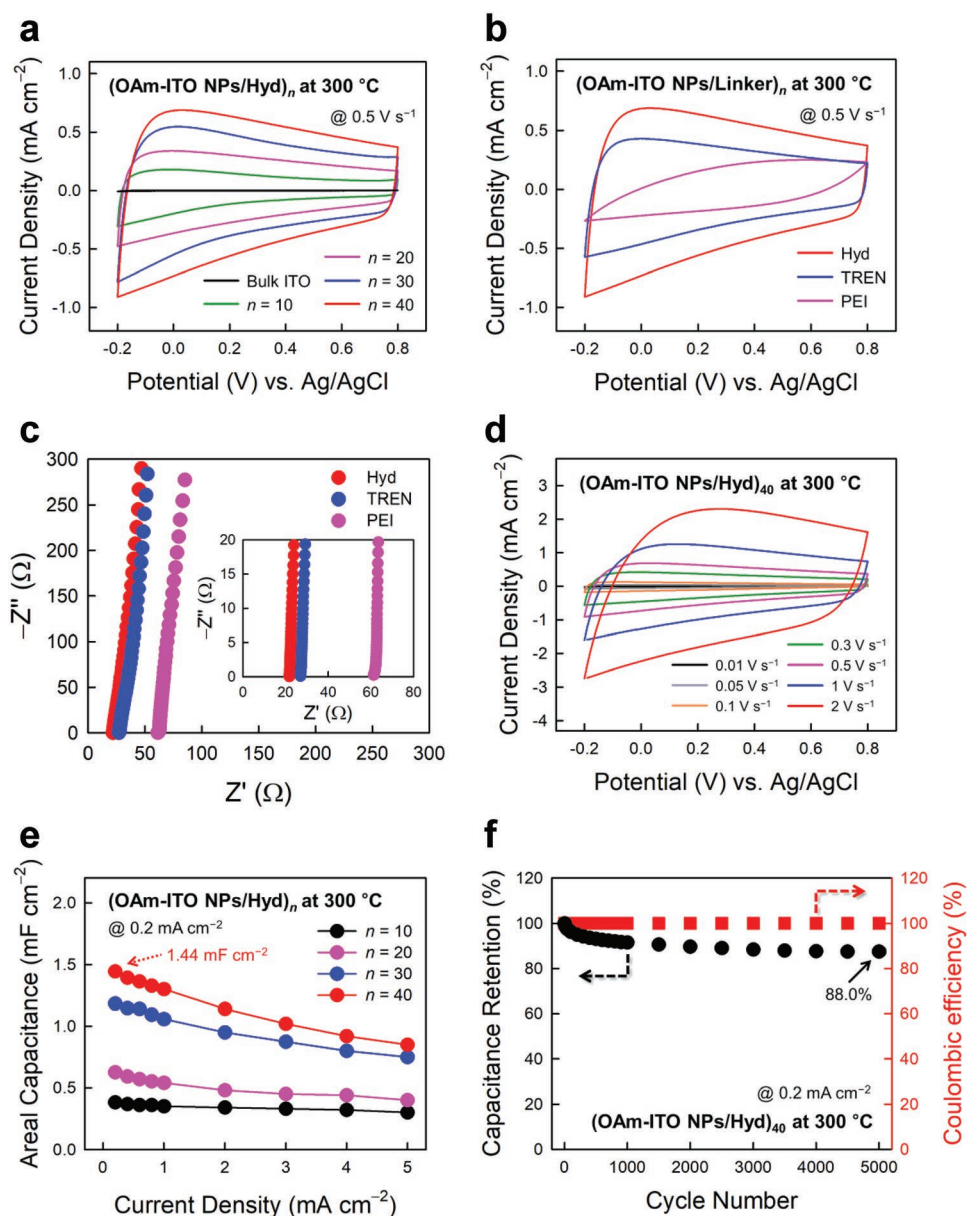
Figure 5. a) CV curves of (OAm–ITO NPs/Hyd)$_n$ multilayers and bulk ITO–sputtered glass acquired at a scan rate of 0.5 V s^{-1} for different bilayer numbers (n). b) CV curves acquired at a scan rate of 0.5 V s^{-1} and c) Nyquist plots of (OAm–ITO NPs/Hyd)$_{40}$, (OAm–ITO NPs/TREN)$_{30}$, and (OAm–ITO NPs/PEI)$_{26}$ multilayers at the same loading amount of ITO NPs. d) CV curves of (OAm–ITO NPs/Hyd)$_{40}$ multilayers with increasing scan rates from 0.01 to 2 V s^{-1}. e) Areal capacitances of (OAm–ITO NPs/Hyd)$_n$ multilayers calculated from GCD profiles at different current densities ranging from 0.2 to 5 mA cm^{-2} as a function of bilayer number. f) Cycling retention (left axis) and Coulombic efficiency (right axis) of (OAm–ITO NPs/Hyd)$_{40}$ multilayers at a current density of 0.2 mA cm^{-2} for 5000 cycles.

increase of electrochemically active surface area of (OAm–ITO NPs/Hyd)$_n$ multilayers. Considering that nanostructured electrodes can provide a larger surface-to-volume ratio than bulk electrodes and consequently a more intimate contact between electrodes and electrolytes,[38] it seems reasonable that (OAm–ITO NPs/Hyd)$_n$ multilayers displayed significantly higher capacitances than bulk ITO films.

We also compared the CV curves of ITO NP–based electrodes with three different organic linkers (i.e., Hyd, TREN, and PEI) to analyze their effects on electrochemical performance. For this comparison, the bilayer numbers (n) of

(OAm–ITO NPs/TREN)$_{30}$ and (OAm–ITO NPs/PEI)$_{26}$ multilayers were adjusted to obtain the same loading amount of electrochemically active ITO NPs with (OAm–ITO NPs/Hyd)$_{40}$ multilayers (Figures S9 and S10, Supporting Information). As shown in Figure 5b, when Hyd linkers were used, the current response level was much higher than that of PEI and TREN linker–based multilayers. These phenomena are closely related to the reduced total resistances in the (OAm–ITO NPs/Hyd)$_{40}$ multilayers because of the increased oxygen vacancy states and the minimized separation distance between neighboring ITO NPs, as mentioned earlier. To further investigate the

ADVANCED
SCIENCE NEWS
www.advancedsciencenews.com

NANO · MICRO
small
www.small-journal.com

total resistances, the frequency responses of (OAm–ITO NPs/Hyd)$_{40}$, (OAm–ITO NPs/TREN)$_{30}$, and (OAm–ITO NPs/PEI)$_{26}$ multilayers were examined by electrochemical impedance spectroscopy (EIS) (Figure 5c). In this case, the equivalent series resistance (ESR) of (OAm–ITO NPs/Hyd)$_{40}$ multilayers was measured to be ≈21.8 Ω, which was relatively lower than that of (OAm–ITO NPs/TREN)$_{30}$ (≈27.0 Ω) and (OAm–ITO NPs/PEI)$_{26}$ multilayers (≈61.3 Ω), indicating the enhanced electron transport properties of the Hyd linker–based multilayers. Additionally, the ESR values showed little change with increasing the bilayer number of (OAm–ITO NPs/Hyd)$_n$ multilayers (Figure S13, Supporting Information).

The CV curves of (OAm–ITO NPs/Hyd)$_n$ multilayers at different scan rates from 0.01 to 2 V s^{-1} demonstrated excellent capacitive behavior. Specifically, their quasirectangular shapes were maintained even at a high scan rate of up to 2 V s^{-1}, implying a good rate capability (Figure 5d and Figure S14 (Supporting Information)). Furthermore, the galvanostatic charge–discharge (GCD) profiles of (OAm–ITO NPs/Hyd)$_n$ multilayers were also recorded as a function of bilayer number with varying current densities from 0.2 to 2 mA cm^{-2} (Figure S15, Supporting Information). The GCD curves displayed a favorable capacitive behavior with symmetric triangular features, indicating typical EDLC behaviors, as already observed in the CV measurements. With increasing current densities from 0.2 to 5 mA cm^{-2}, the areal capacitances of (OAm–ITO NPs/Hyd)$_{40}$ multilayers measured from the GCD curves gradually decreased from 1.44 to 0.80 mF cm^{-2} (Figure 5e). This superior rate capability is attributed to the use of molecular Hyd linkers that can facilitate electron transport within the electrodes by reducing the contact resistance between neighboring ITO NPs. It should be also noted that these areal capacitances of the (OAm–ITO NPs/Hyd)$_n$ multilayers can be further improved by simply increasing the bilayer number (or the loading amount). The (OAm–ITO NPs/Hyd)$_{40}$ multilayers maintained 88.0% of their initial capacitance after 5000 GCD cycles at a current density of 0.2 mA cm^{-2}, signifying a good long-term cycling stability (Figure 5f and Figure S16 (Supporting Information)). Additionally, the Coulombic efficiency, determined by the ratio between the charging time (t_c) and discharging time (t_d) in the GCD profiles, was measured to be almost 100% throughout all GCD cycles.

3. Conclusion

In this study, we demonstrated that solution-processable ITO NP–based TCO electrodes with high transparency, high electrical conductivity, adjustable oxygen vacancies, and complex geometries could be prepared using a unique LbL assembly mediated by the carbon-free molecular Hyd linkers with a strong reducing property. We attributed these characteristics to the Hyd linkers that can generate the oxygen vacancy states within ITO NPs and significantly reduce the contact resistance among ITO NPs owing to their extremely small size. Furthermore, in contrast with the use of PEI or TREN linkers containing hydrocarbons, the use of carbon-free Hyd linkers enables the multilayers to maintain their high optical transmittance even after thermal annealing process. As a result, the

(OAm–ITO NPs/Hyd)$_{40}$ multilayers exhibited a remarkably low sheet resistance of 86 Ω sq^{-1} at an annealing temperature of 300 °C and a high optical transmittance of ≈90%. Additionally, our ITO NP–based TCO electrodes were successfully applied to the high-curvature substrates and possessed a high electrochemical activity (areal capacitance ≈1.44 mF cm^{-2}) based on the large specific surface area. Given that the electrical properties of metal oxide NPs can be enhanced by controlling the oxygen vacancy states and their interparticle distance, we believe that our approach can be effectively applied to the various electrical/electrochemical applications as well as TCO-based displays.

4. Experimental Section

Materials: All chemical reagents used in experiments were purchased from Sigma-Aldrich and used without additional purifications. Solvents, including toluene and ethanol, were purchased from Daejung Chemicals & Metals Co., Ltd. (Republic of Korea).

Synthesis of OAm–ITO NPs: OAm–ITO NPs in toluene were prepared as previously reported.[30] Briefly, indium(III) acetate (6.48 mmol), tin(II) ethylhexanoate (0.72 mmol), OCA (21.6 mmol), OAm (60 mmol), and dioctyl ether (60 mL) were mixed in a three-neck flask under magnetic stirring. The reaction mixture was heated at 80 °C for 1 h under vacuum and then heated at 150 °C for 1 h under an Ar atmosphere. Sequentially, the mixture was heated at 280 °C for 2 h to form the NPs. The resultant solution was cooled to room temperature and centrifuged (8000 rpm, 10 min, 20 °C) several times with excess acetone to remove residual impurities. Finally, the obtained OAm–ITO NP precipitates were dispersed in toluene and centrifuged (6000 rpm, 10 min, 20 °C) to ensure a uniform size distribution.

LbL Assembly of (OAm–ITO NPs/Hyd)$_n$ Multilayers: First, LbL assemblies were carried out in the fume hood for experimental safety. All substrates (i.e., Si wafers, quartz glasses, gold-sputtered Si wafers (for FTIR analysis), QCM electrodes, and ITO-sputtered glasses) were surface-treated using an UV–ozone cleaner (λ ≈ 350 nm) for 10 min. These substrates were subsequently dipped into a solution of NH$_2$-functionalized PEI in ethanol (2 mg mL^{-1}, M_w ≈ 800) for 20 min and then gently washed with pure ethanol to remove weakly adsorbed materials. After drying the residual solvent using a compressed air stream, the PEI-coated substrates were immersed in a solution of OAm–ITO NPs in toluene (10 mg mL^{-1}) for 20 min, washed with pure toluene, and dried under a compressed air stream. Next, the OAm–ITO NP–coated substrates were dipped into a solution of Hyd monohydrate in ethanol (2 mg mL^{-1}) for 20 min, followed by washing with pure ethanol and drying. These dipping cycles were repeated until the desired number of multilayers was obtained. The LbL assembly of (OAm–ITO NPs/PEI)$_n$ and (OAm–ITO NPs/TREN)$_n$ multilayers was performed with the same procedure, except that PEI (2 mg mL^{-1}, M_w ≈ 800) and TREN (2 mg mL^{-1}) dissolved in ethanol were used instead of Hyd solution.

Film Characterization: The size distribution and crystal structure of OAm–ITO NPs were investigated using HR-TEM (Tecnai 20, FEI). XRD patterns of OAm–ITO NPs were obtained using XRD-2500/PC (Rigaku Co.) with Cu K$_\alpha$ radiation (40 kV, 150 mA). XPS analysis of ITO NP films was conducted using X-TOOL (ULVAC-PHI) with Al K$_\alpha$ radiation. To confirm the occurrence of ligand-exchange reactions, vibrational spectra of the multilayers were acquired using a FTIR spectrometer (CARY 600, Agilent Technologies) in ATR mode at room temperature. The collected raw data were plotted after baseline corrections using spectra analyzing software (OMNIC, Nicolet). The qualitative growth and optical bandgap of the multilayers were examined by a UV–visible spectrometer (Lambda 35, Perkin Elmer) in the spectral range from 200 to 1000 nm, and the quantitative growth of the multilayers was measured by QCM (QCM

ADVANCED
SCIENCE NEWS
www.advancedsciencenews.com

NANO · MICRO
small
www.small-journal.com

200, SRS). Mass changes (Δm) were calculated from frequency changes ($-\Delta F$) using the Sauerbrey equation as follows[28]

$$\Delta F \,(\text{Hz}) = -\frac{2F_0^2}{A\sqrt{\rho_q \mu_q}} \times \Delta m \tag{1}$$

In Equation (1), F_0 (≈ 5 MHz) is a fundamental resonance frequency, A is the surface area (cm^2), ρ_q (≈ 2.65 g cm^{-3}) is the density, and μ_q ($\approx 2.95 \times 10^{11}$ g cm^{-1} s^{-2}) is the shear modulus of the QCM electrodes. Consequently, Equation (1) could be simplified by substituting the actual values and expressed as Equation (2)

$$-\Delta F \,(\text{Hz}) = 56.6 \times \Delta m_A \tag{2}$$

where Δm_A indicates the mass change per unit area (µg cm^{-2}). The compositions of the multilayers were analyzed by thermogravimetric analysis (TGA; Q50, TA Instruments) with increasing temperature from 25 to 650 °C at a heating rate of 5 °C min^{-1} under a N$_2$ atmosphere. Finally, the surface morphology and film thickness of the multilayers were observed using FE-SEM (S-4800, Hitachi) and AFM (XE-100, Park System).

Electrical and Optical Measurements: The sheet resistance was obtained by the four-point probe method using Loresta-GP MCP-T610 (Mitsubishi Chemical Analytech). The electrical conductivity was calculated from the measured sheet resistance and film thickness (evaluated by cross-sectional FE-SEM images). The Hall carrier concentration and mobility were examined using a Hall effect measurement system (HMS-3000 and MP55T, Ecopia). Optical transmittance spectra were recorded across a wavelength range from 200 to 1000 nm using a UV–visible spectrometer (Lambda 35, Perkin Elmer).

Electrochemical Measurements: All electrochemical properties of ITO NP–based TCO electrodes were evaluated with an Ivium-n-Stat analyzer (Ivium Technologies, Netherlands) in a three-electrode cell configuration using an aqueous solution of sodium sulfate (Na$_2$SO$_4$, 0.5 mol L^{-1}) as the electrolyte. Ag/AgCl electrode saturated with sodium chloride in deionized water (3 mol L^{-1}) and a platinum wire were used as the reference and counter electrodes, respectively. The commercial ITO–sputtered glass substrates were used as current collectors and the active area of working electrodes was fixed at 2 cm^2. The electrochemical analyses, including CV and GCD measurements, were carried out in the potential range between -0.2 and $+0.8$ V, and EIS measurements were conducted at frequencies ranging from 100 kHz to 0.1 Hz with a perturbation amplitude of 0.01 V. The areal capacitances (C) were calculated from GCD profiles by the following Equation (3)

$$C = \frac{I\Delta t}{\Delta V} \tag{3}$$

where I, Δt, and ΔV represent the applied current density, discharging time, and operating voltage window, respectively.

Supporting Information

Supporting Information is available from the Wiley Online Library or from the author.

Acknowledgements

Conflict of Interest

The authors declare no conflict of interest.

Keywords

[1] J. M. Caruge, J. E. Halpert, V. Wood, V. Bulovic, M. G. Bawendi, *Nat. Photonics* **2008**, *2*, 247.
[2] A. Llordés, G. Garcia, J. Gazquez, D. J. Milliron, *Nature* **2013**, *500*, 323.
[3] M.-G. Kim, M. G. Kanatzidis, A. Facchetti, T. J. Marks, *Nat. Mater.* **2011**, *10*, 382.
[4] K. Ellmer, *Nat. Photonics* **2012**, *6*, 809.
[5] J. Lee, S. Lee, G. Li, M. A. Petruska, D. C. Paine, S. Sun, *J. Am. Chem. Soc.* **2012**, *134*, 13410.
[6] J. Song, S. A. Kulinich, J. Li, Y. Liu, H. Zeng, *Angew. Chem.* **2015**, *127*, 472.
[7] G. Bühler, D. Thölmann, C. Feldmann, *Adv. Mater.* **2007**, *19*, 2224.
[8] J. Lee, M. A. Petruska, S. Sun, *J. Phys. Chem. C* **2014**, *118*, 12017.
[9] Z. Chen, X. Qin, T. Zhou, X. Wu, S. Shao, M. Xie, Z. Cui, *J. Mater. Chem. C* **2015**, *3*, 11464.
[10] S. Bellani, L. Najafi, G. Tullii, A. Ansaldo, R. Oropesa-Nuñez, M. Prato, M. Colombo, M. R. Antognazza, F. Bonaccorso, *J. Mater. Chem. A* **2017**, *5*, 25177.
[11] M. Yarema, S. Pichler, D. Kriegner, J. Stangl, O. Yarema, R. Kirchschlager, S. Tollabimazraehno, M. Humer, D. Häringer, M. Kohl, G. Chen, W. Heiss, *ACS Nano* **2012**, *6*, 4113.
[12] J.-A. Jeong, J. Lee, H. Kim, H.-K. Kim, S.-I. Na, *Sol. Energy Mater. Sol. Cells* **2010**, *94*, 1840.
[13] J. Song, H. Zeng, *Angew. Chem., Int. Ed.* **2015**, *54*, 9760.
[14] E. N. Dattoli, W. Lu, *MRS Bull.* **2011**, *36*, 782.
[15] C. Peng, Y. S. Thio, R. A. Gerhardt, *J. Phys. Chem. C* **2010**, *114*, 9685.
[16] S. Yang, Y. Liu, Y. Hao, X. Yang, W. A. Goddard III, X. L. Zhang, B. Cao, *Adv. Sci.* **2018**, *5*, 1700659.
[17] M. Kim, B. Lee, H. Ju, J. Y. Kim, J. Kim, S. W. Lee, *Adv. Mater.* **2019**, *31*, 1903316.
[18] Y. Jiao, D. Han, Y. Ding, X. Zhang, G. Guo, J. Hu, D. Yang, A. Dong, *Nat. Commun.* **2015**, *6*, 6420.
[19] G. Decher, *Science* **1997**, *277*, 1232.
[20] S. S. Shiratori, M. F. Rubner, *Macromolecules* **2000**, *33*, 4213.
[21] Y. Kim, J. Zhu, B. Yeom, M. D. Prima, X. Su, J.-G. Kim, S. J. Yoo, C. Uher, N. A. Kotov, *Nature* **2013**, *500*, 59.
[22] J.-S. Lee, J. Cho, C. Lee, I. Kim, J. Park, Y.-M. Kim, H. Shin, J. Lee, F. Caruso, *Nat. Nanotechnol.* **2007**, *2*, 790.
[23] Y. Ko, H. Baek, Y. Kim, M. Yoon, J. Cho, *ACS Nano* **2013**, *7*, 143.
[24] S. Cheong, J.-K. Kim, J. Cho, *Nanoscale* **2016**, *8*, 18315.
[25] I. Cho, H. Jung, B. G. Jeong, J. H. Chang, Y. Kim, K. Char, D. C. Lee, C. Lee, J. Cho, W. K. Bae, *ACS Nano* **2017**, *11*, 684.
[26] Y. Ko, M. Kwon, W. K. Bae, B. Lee, S. W. Lee, J. Cho, *Nat. Commun.* **2017**, *8*, 536.
[27] C. H. Kwon, Y. Ko, D. Shin, M. Kwon, J. Park, W. K. Bae, S. W. Lee, J. Cho, *Nat. Commun.* **2018**, *9*, 4479.
[28] Y. Song, D. Kim, S. Kang, Y. Ko, J. Ko, J. Huh, Y. Ko, S. W. Lee, J. Cho, *Adv. Funct. Mater.* **2019**, *29*, 1806584.

[29] I. Cho, H. Jung, B. G. Jeong, D. Hahm, J. H. Chang, T. Lee, K. Char, D. C. Lee, J. Lim, C. Lee, J. Cho, W. K. Bae, *ACS Appl. Mater. Interfaces* **2018**, *10*, 22453.

[30] M. Kanehara, H. Koike, T. Yoshinaga, T. Teranishi, *J. Am. Chem. Soc.* **2009**, *131*, 17736.

[31] M. Mierzwa, E. Lamouroux, P. Durand, M. Etienne, *ChemElectroChem* **2018**, *5*, 397.

[32] D. Zhao, M. Wang, T. Kong, Y. Shang, X. Du, L. Guo, S. Shen, *Mater. Today Chem.* **2019**, *11*, 296.

[33] M. Brahmayya, S. A. Dai, S.-Y. Suen, *RSC Adv.* **2015**, *5*, 65351.

[34] H. Kim, C. M. Gilmore, A. Piqué, J. S. Horwitz, H. Mattoussi, H. Murata, Z. H. Kafafi, D. B. Chrisey, *J. Appl. Phys.* **1999**, *86*, 6451.

[35] T. O. L. Sunde, E. Garskaite, B. Otter, H. E. Fossheim, R. Saeterli, R. Holmestad, M.-A. Einarsrud, T. Grande, *J. Mater. Chem.* **2012**, *22*, 15740.

[36] R. B. H. Tahar, T. Ban, Y. Ohya, Y. Takahashi, *J. Appl. Phys.* **1997**, *82*, 865.

[37] D. V. Talapin, C. B. Murray, *Science* **2005**, *310*, 86.

[38] G. Yu, X. Xie, L. Pan, Z. Bao, Y. Cui, *Nano Energy* **2013**, *2*, 213.